analytical chemistry

Article

pubs.acs.org/ac

Use of Dispersion Imaging for Grating-Coupled Surface Plasmon Resonance Sensing of Multilayer Langmuir−Blodgett Films

Wei-Hsun Yeh and Andrew C. Hillier*

Department of Chemical and Biological Engineering, Iowa State University, Ames, Iowa, United States

Supporting Information

ABSTRACT: We report grating-coupled surface plasmon resonance measurements involving the use of dispersion images to interpret the optical response of a metal-coated grating. Optical transmission through a grating coated with a thin, gold film exhibits features characteristic of the excitation of surface plasmon resonance due to coupling with the nanostructured grating surface. Evidence of numerous surface plasmon modes associated with coupling at both front (gold/air) and back (gold/substrate) grating interfaces is observed. The influence of wavelength and angle of incidence on plasmon coupling can be readily characterized via dispersion images, and the associated image features can be indexed to matching conditions associated with several diffracted orders at both the front and back of the grating. These features collapse onto a set of global dispersion curves when plotted as peak energy versus the grating wavevector, with feature locations clustered according to the refractive index values of the neighboring dielectric material, either air or polycarbonate. Coating of the grating with multilayer arachidic acid films via Langmuir−Blodgett deposition results in red-shifting of some, but not all, of the plasmon features. The magnitude of the shift is a function of the film thickness, wavelength, and angle of incidence. Dispersion images clearly depict the red-shifting and also broadening of the front side features with increasing film thickness. In contrast, little change is observed in features associated with the back-side of the grating. The nature and magnitude of the interaction between the plasmon modes appearing at the front and back sides of the grating are discussed and analyzed in terms of the predicted interactions determined via optical modeling calculations.

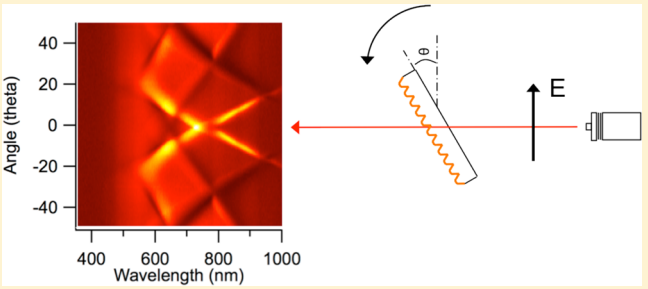

Optical sensors based upon surface plasmon resonance (SPR) have become exceedingly popular analytical tools for thin film and adsorption sensing.[1] One of the key design parameters for SPR sensors is the choice of optical coupler, which is needed to match the momentum of an input light wave to the surface plasmons at a metal/dielectric interface. The most commonly used coupling method is the so-called Kretschmann−Raether configuration, whereby attenuated total internal reflection at the interface of a high refractive index prism is used to generate the matching conditions necessary to excite surface plasmons.[2] An alternative and increasingly attractive approach is one that exploits nanostructured surfaces to couple to surface plasmons.[3] Some examples of nanostructures used for SPR sensing include nanohole arrays,[4] single nanometer-scale holes,[5] nanoslit arrays,[6] nanopyramids,[7] and various grating-type and diffractive nanostructures.[8] One of the most readily accessible nanostructures that can be used to excite surface plasmons are those based upon diffraction gratings.[9] Notably, the very first observation of surface plasmons was made in 1902 by Wood when studying a metallic diffraction grating.[10] Gratings are advantageous in that they are commercially available in a variety of forms, either as optical elements used for spectroscopy or as CDs, DVDs, and blue-ray discs. In addition, custom gratings can be readily fabricated via machining and laser-based interferometry techniques.[8a−e,11]

Grating-based SPR sensing has several key advantages compared to other SPR methods.[1c,12] Gratings represent an inherently information-rich substrate due to surface plasmons appearing not only in the directly reflected or transmitted peaks but also in the various diffracted orders.[11a] In addition, the plasmon response is highly tunable based upon the grating profile. Indeed, changing the amplitude, shape or pitch of the grating has a dramatic effect on the wavelength and shape of the plasmon resonance.[8a,13] Thus, this substrate represents a highly flexible and tunable platform for sensor development.

One of the challenges associated with grating-based SPR platforms involves the fact that the nature of this surface is complex and can lead to the simultaneous excitation of multiple surface plasmons and overlap between those various modes. For example, more than one surface plasmon mode can be excited due to the opportunity for coupling to several diffracted orders from the grating interface.[14] In addition, the two-sided nature of grating couplers allows surface plasmons to be excited at both metal/dielectric interfaces. This means that surface plasmons can exist at both the "front" and "back" sides of the grating. Ultimately, the formation of multiple surface plasmons

Received: January 15, 2013
Accepted: March 22, 2013
Published: March 22, 2013

   dx.doi.org/10.1021/ac400144q | *Anal. Chem.* 2013, 85, 4080−4086

leads to the appearance of additional features and complexity in the optical response, which can complicate interpretation of this data. In order to address the added complexity of grating-coupled SPR, we describe the use of dispersion images to provide a detailed picture of surface plasmon excitation at a model metal-coated grating. Notably, dispersion imaging has been previously used to characterize surface plasmons at various nanostructures[3a] and has been particularly useful in the analysis and control of surface plasmon-coupled emission phenomena.[15]

In this work, an asymmetric grating composed of a plastic/metal/ambient interface is constructed and analyzed via automated angle-scan transmission measurements, which are used to construct dispersion images. Various optical features in this response are analyzed in terms of the associated diffracted orders at the metal/dielectric interface to accurately identify the origin of these features. These data are also compared to results from optical modeling. The impact of a dielectric coating consisting of a multilayer Langmuir–Blodgett film is also examined in terms of the shifts (or lack thereof) of the various plasmon peaks. These results are compared to theoretical predictions based upon optical modeling calculations.

EXPERIMENTAL SECTION

Materials and Reagents. Arachidic acid and chloroform were purchased from Sigma Aldrich (St. Louis, MO). All chemicals and reagents were used as received. Deionized water with electrical resistivity greater than 18 MΩ·cm was used during rinsing and cleaning procedures (NANOPure, Barnstead, Dubuque, IA). Recordable digital versatile discs (DVD-R, 4.7GB) were purchased from Inkjet Art Solutions (Salt Lake City, UT). Gold (99.999%) and Tungsten wire baskets were purchased from Ted Pella, Inc. (Redding, CA).

Grating Construction. Gratings substrates were prepared from commercial DVD-Rs, which were split with a razor blade, cleaned, and then coated with a thin layer of gold, as described previously.[8c] Gold was coated to a thickness of ∼40 nm using a thermal metal evaporator (Benchtop Turbo III, Denton Vacuum). The metal thickness was verified during deposition using a quartz crystal thickness monitor and confirmed postdeposition using a combination of atomic force microscopy and optical absorbance measurements.

Langmuir–Blodgett Deposition. Multilayer films of arachidic acid were deposited onto the gold-coated grating by Langmuir–Blodgett deposition using a computer-controlled deposition trough (Model 610, Nima Technologies). Films of arachidic acid were spread onto a pure water subphase using chloroform as a solvent. Following solvent evaporation, the surface film was compressed to a surface pressure of ∼15 mN m^{-1}. Films were then formed on the grating substrates by automated dip-coating. Gratings were translated at a rate of 1 mm min^{-1} through the air/water interface, and the arachidic acid was replenished between deposition strokes to maintain a constant surface pressure. Film thicknesses were confirmed using a combination of quartz crystal gravimetry, ellipsometry, and atomic force microscopy.

Atomic Force Microscope (AFM) Imaging. AFM images of the sample surfaces were acquired with a Dimension 3100 scanning probe microscope and Nanoscope IV controller (Veeco Metrology, LLC, Santa Barbara, CA). Imaging was performed in tapping mode using silicon TESP7 AFM tips (Veeco Metrology, LLC, Santa Barbara, CA) with a spring constant of ∼70 N m^{-1} and a resonance frequency of ∼280 kHz.

Optical Characterization. All optical transmission measurements were carried out using a custom-built optical system (Figure S.1, Supporting Information). White light from a tungsten-halogen source (Model LS1, Ocean Optics, Dunedin, FL) was collimated using a convex lens with focal length of 150 mm (Newport Corp.). The resulting beam passed through a Glan Thompson polarizer before illuminating the grating sample through a 2 mm diameter aperture. The sample was mounted on a motorized, rotating sample stage (Model PRM1Z8, Thorlabs) for automated alignment and rotation. The transmitted light was collected using a 600 μm optical fiber and recorded with a fiber optic spectrometer (SD2000, Ocean Optics, Inc., Dunedin, FL). Dispersion images were acquired by rotating the sample using the motorized sample stage and synchronizing this rotation with the acquisition of transmission spectra through the spectrometer using a custom Labview code.

Optical Modeling. The rigorously coupled wave analysis (RCWA) method was used to model the optical response of the grating with various coated layers, as described previously.[16] Briefly, diffraction efficiencies were computed for transmitted and reflected light using both transverse magnetic (TM) and transverse electric (TE) incident light as a function of wavelength and angle of incidence. A custom-built code was written in Matlab to perform the computations. The grating geometry was approximated on the basis of fitting AFM images of the grating surface. The surface profile of the grating was represented using two-different shapes, one with a sawtooth profile and the other with a more segmented shape, and both having a pitch of 700 nm and amplitude of 120 nm. Wavelength-dependent refractive index values used in the computations included published values for gold.[17] The polycarbonate substrate was modeled using the Sellmeier equation.[18]

RESULTS AND DISCUSSION

A representative sample geometry used for grating-coupled surface plasmon resonance (GC-SPR) is depicted in Scheme 1. A typical sample consists of an optically transparent substrate (polycarbonate, in this case) on which the grating topology is molded. A thin gold film is coated on one side of the grating in order to support the generation of surface plasmon polaritons

Scheme 1. Schematic of Grating Showing Air/Film/Metal/Polycarbonate Interfaces and Primary Reflected (R_i) and Transmitted (T_i) Modes from Several Diffracted Orders at the Front (Metal/Film) and Back (Metal/Polycarbonate) Grating Interfaces

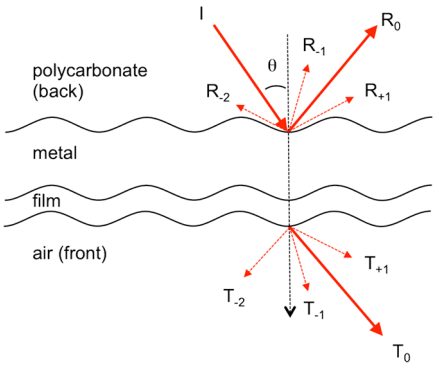

dx.doi.org/10.1021/ac400144q | Anal. Chem. 2013, 85, 4080–4086

(SPPs) at the metal/dielectric interfaces. For sensing applications, a thin film or adsorbate is anchored at the metal/air interface, which changes the local dielectric environment near the metal surface and perturbs the resonance conditions for the SPPs. This generally produces a red-shift in the resonance conditions that can be observed through changes in the transmitted or reflected light.[2a] Coupling to SPPs can occur via several different diffracted orders on both back (gold/polycarbonate) and front (gold/film/air) sides of the grating interface and can be observed in both transmission (T) and reflection (R) modes, as depicted in Scheme 1.

Grating-coupled SPR has been shown to produce enhanced optical transmission at specific wavelengths associated with a matching of the grating wavevector with that of SPPs at the metal/dielectric interface.[8c,19] An example of this enhancement is shown in Figure 1, which depicts a series of p-polarized

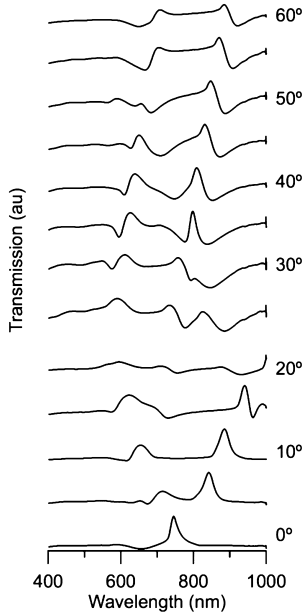

Figure 1. Experimental transmission spectra (p-polarized light) through gold-coated (40 nm) DVD grating as a function of wavelength and angle of incidence.

transmission spectra for light incident on a gold-coated grating as a function of angle of incidence. An enhanced transmission peak is evident at ~750 nm for directly transmitted light (θ = 0°). Changing the angle of incidence shifts the location of the enhanced transmission peak, as well as produces additional features in the transmission spectra. Indeed, several of the peaks appearing in Figure 1 can be indexed according to specific diffracted orders coupling to SPPs in the metal film, and the change in these peak positions with angle of incidence has been previously noted.[8c,19a] A closer look at the various transmission spectra shows fine structure, however, that is difficult to immediately identify.

A more complete picture of the transmission response, and greater detail about the subtle features observed in the spectra, can be more readily seen in the form of a dispersion image (Figure 2A). This image represents a dense compilation of experimentally measured spectra taken over a range of incident angles. These data were acquired by recording p-polarized transmission spectra every 0.5° while rotating the sample grating about its axis using a computer controlled rotation

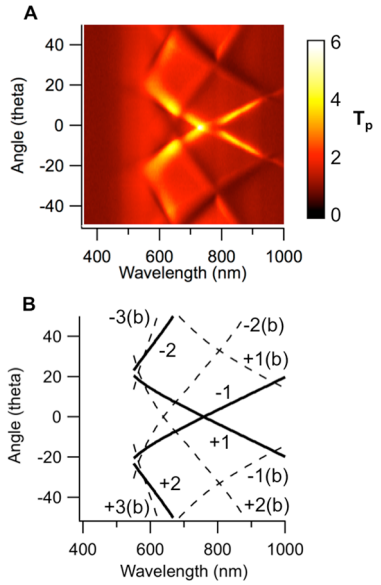

Figure 2. (A) Dispersion image showing a compilation of experimental p-polarized transmission data (T_p) versus wavelength and angle of incidence through a gold-coated grating. The data has been normalized by dividing by the s-polarized transmission spectra of a flat surface with the same gold thickness. (B) Calculated SPR matching conditions for gold-coated grating having a 700 nm pitch. The matching conditions and corresponding diffraction orders are identified with solid and dashed lines. All backside (gold/polycarbonate) diffraction features are identified with (b) and dashed lines. The remaining front side (gold/air) features are identified with solid lines.

stage. The image was normalized by dividing it by the s-polarized transmission spectra of a flat, gold-coated surface with the same gold thickness. Within this dispersion image appears a series of crossing lines of either enhanced (light) or suppressed (dark) intensity. At the center of the image, for example, is a pair of light-colored features in the form of an x-pattern associated with the most intense, enhanced light transmission. These features correspond to SPPs generated at the gold/air interface through coupling to the grating's ± 1 diffracted orders (the +1 order has a negative slope and the −1 order has a positive slope).[8c] Additional light and dark lines are also seen throughout the image. These additional features are also SPPs, which are generated through coupling to various other diffracted orders at either the front (gold/air) or the back (gold/polycarbonate) sides of the grating (vide infra).

Identifying the specific location (front or back of grating) and diffracted orders associated with each of these features can be achieved by indexing them with respect to the grating (k_{gr}) and surface plasmon (k_{sp}) wavevectors. The matching condition between the SPP and a grating is given by:

$$k_{sp} = \frac{2\pi}{\lambda}\sqrt{\frac{\varepsilon'_M\varepsilon_D}{\varepsilon'_M + \varepsilon_D}} = \frac{2\pi}{\lambda}n\sin\theta + m\frac{2\pi}{\Lambda} = k_{gr} \quad (1)$$

where λ is the wavelength of light, ε'_M is the real part of the metal's dielectric constant, ε_D is the dielectric constant of the neighboring layer (polycarbonate or air), n is the refractive index of the incident medium (air), θ is angle of incidence, m is an integer (0, ±1, ±2, ...) indicating the diffracted order, and Λ is the grating pitch.[1b,2a,9] Using this formula, the dispersion relations for SPP matching in a gold film can be determined for the various diffracted orders. Figure 2B depicts these relations

dx.doi.org/10.1021/ac400144q | Anal. Chem. 2013, 85, 4080−4086

for several diffracted orders corresponding to the front (gold/air, solid lines) and back (gold/polycarbonate, dashed lines) of the grating. The primary front side feature of note is the matching associated with the +1 and −1 diffracted orders. As noted earlier, these correspond to the largest enhanced transmission features in the experimental dispersion image (Figure 2A). In addition, there are features associated with coupling to the ±2 diffracted orders at the front side of the grating. These appear as enhanced transmission at larger angles and lower wavelengths in the experimental data. The majority of the other features in the dispersion images, which are primarily dark features, can be associated with SPPs generated at the back or polycarbonate/gold side of the grating (as noted by dashed lines in Figure 2B). All of these back-side SPPs appear as reduced transmission or valleys in the experimental dispersion images.

The various features associated with the front and back-side SPPs can also be considered in terms of the overall dispersion relations as described in eq 1. In particular, if one plots the matching conditions for the SPPs in terms of the plasmon energy (in eV) versus the grating wavevector (in nm^{-1}), the front and back-side features all collapse onto two curves, distinguished by the refractive index value of the material at the specific metal/dielectric interface. Figure 3 shows such a plot,

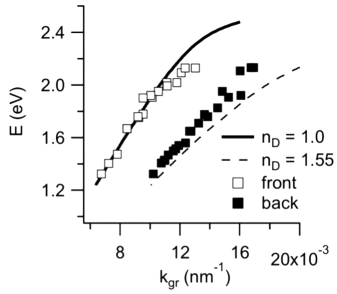

Figure 3. Plot of peak energy (E) versus grating wavevector (k_{gr}) for matching conditions identified in Figure 2B for refractive index values of n_D = 1 (air, solid line) and 1.55 (polycarbonate, dashed line). Data points corresponding to front-side (open squares) and back-side (solid squares) features are also plotted.

where the calculated results from Figure 2B have been recast in terms of the peak energy (E) versus the grating wavevector (k_{gr}).[20] All diffracted orders associated with SPPs at the metal/air interface collapse onto the line associated with the dielectric constant for air (n_D = 1, solid line), while all those associated with the metal/polycarbonate interface collapse onto the line associated with a refractive index of $n_D \sim 1.55$ (dashed line), which is approximately the value reported for polycarbonate in the visible spectrum.[18] In addition, when data from the light (open squares) and dark (filled squares) features in the experimental data in Figure 2A are plotted in Figure 3, they all fall on either the front or back-side curves, corresponding to the refractive index of the nearest dielectric material.

Although the comparison between the SPP matching condition (eq 1) and the experimental results showed good agreement in terms of feature location, subtle details in the experimental data, such as the intensity of the transmitted light or details of the regions where front and back-side features overlap, cannot be represented by this equation. In order to more fully explore the nature of the various features in the dispersion image, a simulation of the optical transmission through a model grating structure was performed. Two different grating shapes were examined. Both shapes are approximations of the measured profile of the grating surface (Figure S.2, Supporting Information). The first modeled topology was a simple sawtooth profile having the same pitch and amplitude as the sample grating. The structure in the optical model was constructed with a polycarbonate base ($n_D \sim$ 1.55), a gold film with a thickness of 40 nm, and an ambient environment of air. A second profile was constructed with a sharper segmented shape to more closely approximate the experimental profile. Both the sawtooth and segmented profile are shown as insets in Figure 4.

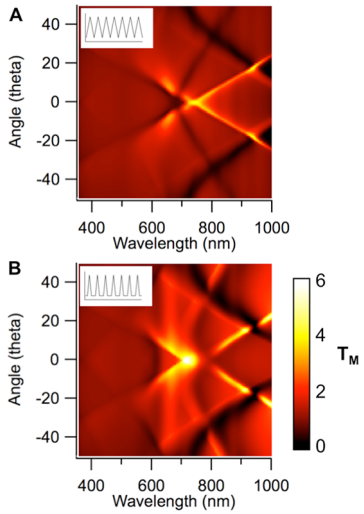

Figure 4. Computed dispersion images for transverse magnetic (T_M) light through two different grating profiles having a 700 nm pitch and 120 nm amplitude with a 40 nm gold layer: (A) sawtooth profile and (B) segmented profile. The surface profiles for each image are identified in the insets.

The optical response of these gratings was computed using the rigorously coupled wave analysis (RCWA) method.[16] The results are shown for transverse magnetic (TM) polarized light through the grating structure, divided by transverse electric (TE) polarized light through a flat, gold-coated surface. The upper image (Figure 4A) is for the sawtooth, and the lower image (Figure 4B) is for the segmented profile. The computed transmission images have numerous features in common with the experimental results (Figure 2A). Notably, the location and intensity of the bright crossing lines associated with the ±1 diffracted peaks are in approximately the same location and exhibit a similar magnitude of enhancement (with $T_{M,max} \sim 5$). For the sawtooth profile (Figure 4A), the enhanced transmission features associated with the ±1 diffracted orders are continuous until they intersect with the ±2 back-side peaks at ~650 nm, where the intensity is extinguished. This behavior is also observed in the experimental data. However, in the experimental data, an additional drop in the light enhancement for the ±1 order features is observed at ~750 nm, where a vertical energy gap appears. This energy gap is consistent with behavior associated with coupling of SPPs to higher order harmonics in the surface periodicity (more precisely, a surface possessing an additional grating wavevector at twice that coupling to the SPP), as has been reported previously.[21] Notably, if one closely examines the model results from the segmented profile (Figure 4B), which possesses a more significant harmonic component in its profile, a similar energy

dx.doi.org/10.1021/ac400144q | Anal. Chem. 2013, 85, 4080−4086

gap also appears at ~750 nm. In addition to these features, the location and orientation of the other peaks and valleys in the simulated images are quite similar to the measured image. Notably, all of these features can be associated with the excitation of SPPs at either the front (gold/air) or back (gold/polycarbonate) sides of the grating. Of these modeled responses, the experimental results more closely follow the behavior of the segmented profile in Figure 4B.

We, and others, have previously demonstrated that enhanced transmission peaks associated with grating-coupled surface plasmon resonance can be used to quantify the thickness of adsorbed thin films or changing dielectric media.[8c,14,19,22] In order to investigate the impact of thin, coated films on the various transmission features observed in Figure 2, we constructed multilayer films of arachidic acid. Langmuir–Blodgett film deposition was used in order to controllably fabricate films of varying thickness. Arachidic acid was spread onto a deionized water subphase from a chloroform solution and deposited at a fixed film pressure (Figure S.3, Supporting Information). The arachidic acid monolayer was compressed to a deposition pressure of ~15 mN m^{-1}. Film coating was then performed by dipping the grating substrate through the arachidic acid monolayer at the air/water interface. Multiple layers were formed by sequential dipping at this film pressure.

The typical response of the enhanced transmission peaks to increasing adsorbed film thickness is to produce a red-shift in the peak positions. This is clearly seen for the transmission peak associated with the −1 order (Figure 5) at two different

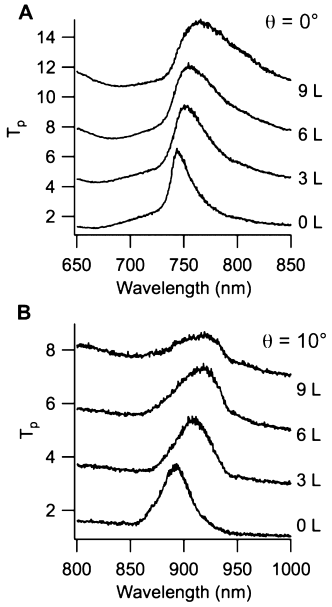

Figure 5. Transmission spectra measured at an angle of incidence of (A) 0° and (B) 10° through gold-coated grating with Langmuir–Blodgett films of arachidic acid at 0, 3, 6, and 9 layer (L) thicknesses. The spectra have been offset in the vertical direction for clarity.

angles of incidence. At θ = 0°, films of 0, 3, 6, and 9 layers of arachidic acid are shown, where each layer corresponds to a bilayer of arachidic acid that forms during a dipping stroke down and back up through the monolayer.[23] The addition of these films produces a red-shifting and broadening of the transmission peak (Figure 5A). A similar red-shifting and broadening is seen when this peak is measured at an incident angle of θ = 10° (Figure 5B).

A quantitative comparison of the peak shifts is illustrated in Figure 6, where the shift in the transmission peak position is

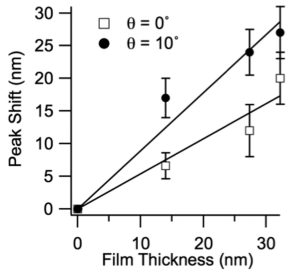

Figure 6. Comparison of the shift in enhanced transmission peaks (from Figure 5) versus film thicknesses (as determined by spectroscopic ellipsometry) at angles of incidence of 0° and 10° for arachidic acid multilayers.

plotted versus the film thickness. The film thicknesses were measured using ellipsometry. According to the ellipsometry results, the average thickness of the arachidic acid layer formed during a single down/up dipping stroke is ~4.5 nm, which is consistent with a bilayer of arachidic acid being deposited (a Y-type film).[24] Literature reports for a single arachidic acid layer give a thickness of between 2.2 and 2.8 nm,[25] which is approximately half the measured thickness and consistent with the formation of a bilayer. The thickness sensitivity of the plasmon peak shifts is ~0.55 nm shift/nm thickness at θ = 0° and ~0.9 nm shift/nm thickness at θ = 10°. These values are similar to previous measurements of thin organic films[8c,14] and consistent with the fact that the magnitude of the peak shifts increases at higher resonant wavelengths, which is the case for the higher sensitivity of the m = −1 peak at θ = 10° versus at θ = 0°.[14,26]

Although the enhanced transmission peak associated with the −1 diffracted order red-shifts in the presence of an adsorbed film as one would expect, the other transmission features appearing throughout the transmission spectrum do not all behave similarly. A more complete picture of the transmission response can be seen with dispersion images of the surface with various film coatings. The shifts (and lack thereof) can be seen most clearly through the use of subtraction images. Figure 7 depicts two such images. Figure 7A shows an image created by subtracting the bare substrate image (Figure 2A) from the dispersion image after deposition of a 3L film (Figure S4B, Supporting Information). This subtraction image will show high contrast, and a blue followed by yellow/red stripes where there has been a red shift in the peaks. Figure 7A shows these features primarily along the ±1 diffracted orders associated with the front side of the grating. A smaller, yet still noticeable, contrast change is seen at the ±2 front side peaks. Very little change is seen at the back-side peaks. This behavior is even more evident when plotting the subtraction image created from the dispersion image from the 6L layer film minus the bare substrate (Figure S4C, Supporting Information). In this image, strong blue to red contrast is observed along the ±1 and ±2 front side features, with a much smaller change along the back-side features.

The influence of a film on the front side (gold/air) interface on the location of the various SPP features can also be more clearly seen by the use of the matching relation in eq 1. The addition of a film on the front gold/air interface has the effect of increasing the effective refractive index at that interface from

dx.doi.org/10.1021/ac400144q | Anal. Chem. 2013, 85, 4080–4086

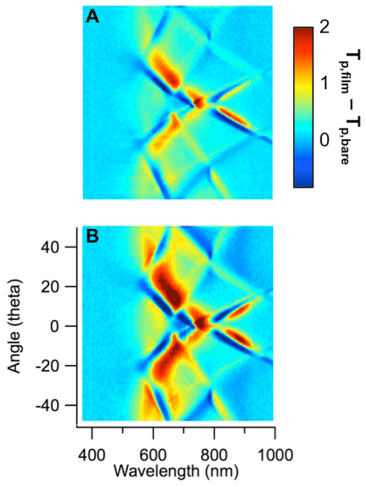

Figure 7. Difference ($T_{p,film} - T_{p,bare}$) images created by taking dispersion images of the (A) 3 layer and (B) 6 layer films and subtracting the bare or uncoated grating. High contrast (red to blue) regions on this image indicate significant red-shifting of the associated dispersion features on the film-coated samples.

a value of that for air (n_D = 1), to a larger value. If one considers how that behavior impacts the SPP coupling conditions as described by eq 1, it produces a red-shift in all of the SPPs. This is shown in Figure 8A, which plots the front side peaks

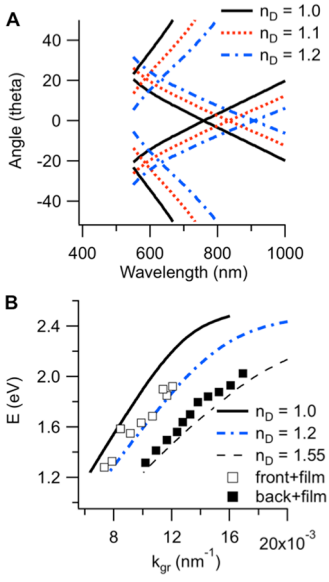

Figure 8. (A) Calculated SPR matching conditions for front-side peaks as a function of refractive index of the surrounding dielectric (n_D). (B) Plot of peak energy versus grating wavevector for refractive index values of 1.0 (air), 1.2, and 1.55 (polycarbonate). Data points for 12 L arachidic acid film on grating for front-side (open squares) and back-side (solid squares) features are also shown.

associated with the ±1 and ±2 diffracted orders for refractive index values of 1, 1.1, and 1.2 for the neighboring dielectric. All of these peaks red-shift with increasing refractive index value. When plotted as energy (E) versus grating wavevector (k_{gr}) (Figure 8B), the result of a changing dielectric constant is the appearance of a single new dispersion curve for each refractive index. Thus, the effect of a film is to increase the effective refractive index of the air/gold interface, which shifts the entire set of front-side plasmon peaks to longer wavelengths (or lower energies). Notably, under conditions where the plasmon decay length within the metal is small, such as due to the lack of optical symmetry at the front and back metal surfaces, the plasmons that form at the front and back side do not communicate. In this circumstance, the back-side peaks would be unaffected by the presence of a film on the front side of the grating, which would support the observed behavior where the back-side peaks do not appear to shift in the presence of the arachidic acid films. Indeed, if one considers experimental results from a 12 L arachidic acid film, the front and back-side features exhibit this behavior. In Figure 8B, the positions of several front side peaks are plotted (open squares) and they all fall nearly along the curve for an effective refractive index of n_D = 1.2, as opposed to falling on the n_D = 1.0 line without the film. In contrast, the back-side peaks (filled squares) still remain near the line corresponding to the higher refractive index of the polycarbonate (n_D = 1.55). Notably, there are conditions, such as in the presence of a very thin metal layer or with a symmetric interface that can support long-range plasmons, where the front and back-side SPPs would interact and both would be impacted by changes in the dielectric environment on the other side of the grating. However, that does not appear to be the case here.

CONCLUSIONS

Surface plasmon resonance sensors using nanostructured surfaces, including diffraction gratings, have become an increasingly popular alternative to the more traditional prism-type couplers. The ability to fabricate nanostructures with well-defined surface topologies allows for fine-tuning of the optical response and a greater ability to control the nature of the coupling to surface plasmons. With this added control, however, comes an added complexity. For example, multiple features, including multiple peaks and valleys, often appear in the optical response of grating-coupled SPR. These additional features are associated with the excitation of several surface plasmon modes, which can be due to the two-sided nature of the grating and also to excitation via higher diffracted orders.

This study focused on understanding the complex optical response that can result from a grating-coupler scheme for surface plasmon resonance sensing. For transmission-based sensing, surface plasmons existing at both the front and back sides of the grating can appear as features, either peaks or valleys, in the transmission spectrum. Interpretation of these features can be assisted through the use of dispersion images, which plot the transmission spectrum as a function of angle of incidence. Combined with optical modeling, we have shown how the features in these dispersion images can be directly indexed to specific plasmon modes, including the associated diffraction order and the interface (front or back side) that the surface plasmon exists. In addition, the sensitivity of these features to changes in the local refractive index, such as via the deposition of thin films, is highly dependent upon the location of the refractive index change. For the deposition of thin films on the metal/ambient or "front-side" of the grating, only the front side features exhibited the characteristic red-shifting. Features in the optical spectrum associated with metal/substrate interface or "back-side" of the grating did not shift in the presence of film formation on the grating's front side. For an asymmetric grating, like the one used here, this would be the generally observed behavior. However, for a grating in which the wave functions of the surface plasmons at the front and back-side interfaces overlapped, such as with a symmetric

dx.doi.org/10.1021/ac400144q | Anal. Chem. 2013, 85, 4080−4086

grating or for one with an exceedingly thin metal film, one would expect interaction between front and back-side plasmons.

■ ASSOCIATED CONTENT

Supporting Information

Additional information as noted in text. This material is available free of charge via the Internet at http://pubs.acs.org.

■ AUTHOR INFORMATION

Corresponding Author

*E-mail: hillier@iastate.edu.

Notes

The authors declare no competing financial interest.

■ ACKNOWLEDGMENTS

The authors would like to thank Joseph Petefish for his assistance with ellipsometry measurements. This work was supported by the National Science Foundation (Grants CHE 0809509 and 1213582).

■ REFERENCES

(1) (a) Homola, J. *Anal. Bioanal. Chem.* **2003**, *377*, 528−539. (b) Homola, J. *Chem. Rev.* **2008**, *108*, 462−493. (c) Homola, J.; Yee, S. S.; Gauglitz, G. *Sens. Actuators, B* **1999**, *54*, 3−15.

(2) (a) Knoll, W. *Annu. Rev. Phys. Chem.* **1998**, *49*, 569−638. (b) Kretschmann, E.; Raether, H. *Z. Naturforsch., A: Phys. Sci.* **1968**, *A 23*, 2135.

(3) (a) Barnes, W. L.; Dereux, A.; Ebbesen, T. W. *Nature* **2003**, *424*, 824−830. (b) Stewart, M. E.; Anderton, C. R.; Thompson, L. B.; Maria, J.; Gray, S. K.; Rogers, J. A.; Nuzzo, R. G. *Chem. Rev.* **2008**, *108*, 494−521.

(4) (a) Brolo, A. G.; Arctander, E.; Gordon, R.; Leathem, B.; Kavanagh, K. L. *Nano Lett.* **2004**, *4*, 2015−2018. (b) Liu, Y.; Bishop, J.; Williams, L.; Blair, S.; Herron, J. *Nanotechnology* **2004**, *15*, 1368−1374.

(5) Rindzevicius, T.; Alaverdyan, Y.; Dahlin, A.; Hook, F.; Sutherland, D. S.; Kall, M. *Nano Lett.* **2005**, *5*, 2335−2339.

(6) Jung, Y. S.; Sun, Z.; Wuenschell, J.; Kim, H. K.; Kaur, P.; Wang, L.; Waldeck, D. *Appl. Phys. Lett.* **2006**, *88*, 243105.

(7) Chung, P. Y.; Lin, T. H.; Schultz, G.; Batich, C.; Jiang, P. *Appl. Phys. Lett.* **2010**, *96*, 261108.

(8) (a) Adam, P.; Dostalek, J.; Homola, J. *Sens. Actuators, B* **2006**, *113*, 774−781. (b) Singh, B. K.; Hillier, A. C. *Anal. Chem.* **2006**, *78*, 2009−2018. (c) Singh, B. K.; Hillier, A. C. *Anal. Chem.* **2008**, *80*, 3803−3810. (d) Tian, S. J.; Armstrong, N. R.; Knoll, W. *Langmuir* **2005**, *21*, 4656−4660. (e) Yu, F.; Tian, S. J.; Yao, D. F.; Knoll, W. *Anal. Chem.* **2004**, *76*, 3530−3535. (f) Dou, X.; Chung, P. Y.; Jiang, P.; Dai, J. L. *Appl. Phys. Lett.* **2012**, *100*, 041116. (g) Dou, X.; Phillips, B. M.; Chung, P. Y.; Jiang, P. *Opt. Lett.* **2012**, *37*, 3681−3683.

(9) Raether, H. *Surface plasmons on smooth and rough surfaces and on gratings*; Springer-Verlag: Berlin; New York, 1988; 136 p.

(10) (a) Wood, R. W. *Proc. Phys. Soc. London* **1902**, *18*, 269. (b) Wood, R. W. *Phys. Rev.* **1935**, *48*, 928−936.

(11) (a) Dostalek, J.; Homola, J.; Miler, M. *Sens. Actuators, B* **2005**, *107*, 154−161. (b) Hutley, M. C. *Diffraction Gratings*; Academic Press: London, 1982.

(12) Dostalek, J.; Homola, J. *Sens. Actuators, B* **2008**, *129*, 303−310.

(13) (a) Kitson, S. C.; Barnes, W. L.; Bradberry, G. W.; Sambles, J. R. *J. Appl. Phys.* **1996**, *79*, 7383−7385. (b) Zhang, N.; Schweiss, R.; Zong, Y.; Knoll, W. *Electrochim. Acta* **2006**, *52*, 2869−2875.

(14) Yeh, W.-H.; Kleingartner, J.; Hillier, A. C. *Anal. Chem.* **2010**, *82*, 4988−4993.

(15) (a) Knoll, W.; Philpott, M. R.; Swalen, J. D. *J. Chem. Phys.* **1981**, *75*, 4795−4799. (b) Toma, M.; Toma, K.; Adam, P.; Homola, J.; Knoll, W.; Dostalek, J. *Optics Express* **2012**, *20*, 14042−14053.

(16) (a) Lalanne, P.; Morris, G. M. *J. Opt. Soc. Am. A* **1996**, *13*, 779−784. (b) Moharam, M. G.; Grann, E. B.; Pommet, D. A.; Gaylord, T. K. *J. Opt. Soc. Am. A* **1995**, *12*, 1068−1076. (c) Moharam, M. G.; Pommet, D. A.; Grann, E. B.; Gaylord, T. K. *J. Opt. Soc. Am. A* **1995**, *12*, 1077−1086.

(17) Johnson, P. B.; Christy, R. W. *Phys. Rev. B* **1972**, *6*, 4370−4379.

(18) Kasarova, S. N.; Sultanova, N. G.; Ivanov, C. D.; Nikolov, I. D. *Opt. Mater.* **2007**, *28*, 1481−1490.

(19) (a) Gurel, K.; Kaplan, B.; Guner, H.; Bayindir, M.; Dana, A. *Appl. Phys. Lett.* **2009**, *94*, 233102. (b) Nazarova, D.; Mednikarov, B.; Sharlandjiev, P. *Appl. Opt.* **2007**, *46*, 8250−8255.

(20) Andrew, P.; Barnes, W. L. *Science* **2004**, *306*, 1002−1005.

(21) (a) Chen, Z.; Hooper, I. R.; Sambles, J. R. *J. Opt. A: Pure Appl. Opt.* **2008**, *10*, 015007. (b) Barnes, W. L.; Preist, T. W.; Kitson, S. C.; Sambles, J. R. *Phys. Rev. B* **1996**, *54*, 6227−6244. (c) Barnes, W. L.; Preist, T. W.; Kitson, S. C.; Sambles, J. R.; Cotter, N. P. K.; Nash, D. J. *Phys. Rev. B* **1995**, *51*, 11164−11167. (d) Kitson, S. C.; Barnes, W. L.; Bradberry, G. W.; Sambles, J. R. *J. Appl. Phys.* **1996**, *79*, 7383−7385. (e) Fischer, B.; Fischer, T. M.; Knoll, W. *J. Appl. Phys.* **1994**, *75*, 1577−1581.

(22) (a) Baba, A.; Tada, K.; Janmanee, R.; Sriwichai, S.; Shinbo, K.; Kato, K.; Kaneko, F.; Phanichphant, S. *Adv. Funct. Mater.* **2012**, *22*, 4383−4388. (b) Dou, X.; Phillips, B. M.; Chung, P.-Y.; Jiang, P. *Opt. Lett.* **2012**, *37*, 3681−3683. (c) Janmanee, R.; Baba, A.; Phanichphant, S.; Sriwichai, S.; Shinbo, K.; Kato, K.; Kaneko, F. *ACS Appl. Mater. Interfaces* **2012**, *4*, 4270−4275. (d) Monteiro, J. P.; Ferreira, J.; Sabat, R. G.; Rochon, P.; Leite Santos, M. J.; Girotto, E. M. *Sens. Actuators, B* **2012**, *174*, 270−273. (e) Yeh, W.-H.; Petefish, J. W.; Hillier, A. C. *Anal. Chem.* **2011**, *83*, 6047−6053.

(23) Bourdieu, L.; Silberzan, P.; Chatenay, D. *Phys. Rev. Lett.* **1991**, *67*, 2029−2032.

(24) Kurnaz, M. L.; Schwartz, D. K. *J. Phys. Chem.* **1996**, *100*, 11113−11119.

(25) Viswanathan, R.; Schwartz, D. K.; Garnaes, J.; Zasadzinski, J. A. N. *Langmuir* **1992**, *8*, 1603−1607.

(26) Homola, J.; Koudela, I.; Yee, S. S. *Sens. Actuators, B* **1999**, *54*, 16−24.